Electrical Power and Energy Systems 172 (2025) 111225

Contents lists available at ScienceDirect

International Journal of Electrical Power and Energy Systems

journal homepage: www.elsevier.com/locate/ijepes

Optimal energy storage configuration for power quality enhancement in active distribution networks with coordinated PV operation

Yang Wang [a,*], Jiaqi Duan [a], Zhuocheng Li [b], Xianyong Xiao [a], Xiang Zhou [a], Hengchen Yang [a], Jiajia Yang [c]

[a] College of Electrical Engineering, Sichuan University, Chengdu 610044, China
[b] State Grid Sichuan Electric Power Company, Chengdu 610041, China
[c] College of Science and Engineering, James Cook University, Townsville 4811, Australia

ARTICLE INFO

Keywords:
ESS configuration
Active distribution network
Muti-phase optimal harmonic power flow
Power quality

ABSTRACT

The extensive integration of renewable energy sources and power electronic devices in active distribution networks (ADNs) has created substantial power quality challenges. Although energy storage systems (ESSs) are considered a key solution, determining optimal ESS locations and capacities remains an unresolved issue. To tackle this problem, this paper develops a bi-level ESS configuration framework. The upper-level model minimizes ESS configuration costs by optimizing location selection and capacity sizing, where the lower-level model formulates a multi-phase optimal harmonic power flow (MPOHPF) problem, aiming to minimize the power loss in the network and keep voltage deviations, harmonic distortions, and voltage unbalance within standard limits. However, the coupling effects between nodes in ADNs and the inclusion of harmonic variables significantly increase the complexity of solving the bi-level model. Therefore, this paper further introduces a candidate node selection strategy based on their contributions to power quality indices, which efficiently narrows down the configuration space. Furthermore, the lower-level model is transformed into a convex quadratic constrained quadratic program by substituting power flow equations with current injection equations. An alternating iterative algorithm is then applied to optimize and compute power flows iteratively, ensuring both convergence and computational efficiency. Finally, the proposed method is comprehensively verified using a 162-node three-phase four-wire distribution network.

1. Introduction

1.1. Background and motivation

With the widespread integration of renewable energy sources and power electronic devices, active distribution networks (ADNs) are facing growing challenges related to power quality [1]. Overvoltage and undervoltage issues have become particularly prominent, especially in distribution systems characterized by high R/X ratios. During daytime hours, peak photovoltaic (PV) generation can lead to excessive voltage rise, whereas the absence of PV output at night, combined with elevated load demand, often results in voltage drops [2]. In addition, the proliferation of non-linear loads, such as variable frequency drives used in industrial and commercial customers and smart home appliances, introduces significant harmonic currents, thereby aggravating voltage harmonic distortion [3]. Moreover, the simultaneous presence of single-phase PV units and unbalanced loads intensifies three-phase voltage imbalance [4], further compromising the overall power quality of the network.

Although mature mitigation strategies have been developed for individual power quality issues, their effectiveness is confined to specific aspects of the problem. For instance, static var compensators dynamically regulate reactive power to mitigate voltage fluctuations [5]; on-load tap changers achieve global voltage control by adjusting transformer tap positions [6]; and active power filters are primarily employed for harmonic suppression [7]. However, none of the above compensation devices are capable of simultaneously addressing the diverse power quality challenges present in ADNs. While coordinated control of multiple devices offers a theoretical pathway to comprehensive mitigation, practical implementation is hindered by disparities in device response characteristics, conflicting control objectives, and the high capital and operational costs associated with multi-device deployment.

* Corresponding author.
E-mail address: fwang@scu.edu.cn (Y. Wang).

https://doi.org/10.1016/j.ijepes.2025.111225
Received 29 May 2025; Received in revised form 24 August 2025; Accepted 30 September 2025
Available online 15 October 2025

In contrast, energy storage systems (ESSs) offer a more integrated solution for power quality enhancement. By regulating active power output, ESS can directly mitigate voltage fluctuations [8]. Moreover, thanks to their fully controllable power electronic interfaces, ESS are inherently capable of suppressing harmonics and compensating for three-phase imbalances [9]-[10]. Nevertheless, given the substantial investment required for ESS deployment, it is essential to strategically determine their optimal configuration within the ADNs to maximize their effectiveness and economic return. Addressing this optimization challenge forms the central focus of the present study.

1.2. Literature review

Currently, the optimal configuration of ESS is typically formulated using either single-level or bi-level optimization models. Compared with single-level approaches, bi-level optimization introduces an additional layer of operational decision-making. Typically, the upper level determines the location and capacity of ESS installations, while the lower level focuses on optimizing their operational strategies. This structure enables coordination across time scales and verifies configuration with operation. For instance, [11–14] developed bi-level planning-operation models where the upper level determines ESS capacity and siting, while the lower level optimizes charging and discharging strategies, effectively reducing network losses and total lifecycle costs. In scenarios with high PV penetration, the upper-level models aim to minimize economic costs, enhance supply reliability [15], and maximize the integrated benefits of multiple stakeholders [16,17], while the lower-level models focus on minimizing operational scheduling costs through optimal ESS operation. These approaches improve renewable energy integration while maintaining economic feasibility. However, studies in [11–17] did not incorporate power quality improvement as an explicit objective.

To fully leverage the potential of ESS in improving power quality, [18] proposed a bi-level optimization approach for ESS, where the upper level aims to minimize wind curtailment and power loss while enhancing voltage stability, and the lower level maximizes market revenue, thereby improving both loadability and voltage stability. In [19], a bi-level framework was developed, in which the upper level determines the optimal ESS capacity by maximizing lifecycle net present value, while the lower level maximizes the combined operating revenue from time-of-use arbitrage and power quality services, yielding configurations that balance investment efficiency and operational performance. In [20], renewables and ESS were treated as an integrated resource: the upper level minimizes operating cost, voltage deviation, and total harmonic distortion to optimize network operation, and the lower level maximizes total revenue from participation in ancillary service markets, improving economic efficiency and reducing harmonic distortion. Reference [21] addressed overvoltage under high renewable penetration with a bi-level model where the upper level minimizes voltage deviation across the network to size ESS, and the lower level derives the operating strategy by minimizing the charge and discharge power required for voltage regulation. Further studies in [22–25] focused on bi-level optimization in PV-rich distribution networks. In [22,23], ESS siting and sizing were handled at the upper level, while the lower-level optimized charge/discharge schedules, accounting for cost and load fluctuations, thereby improving voltage stability and overall grid performance. In [24,25], upper-level objectives include minimizing voltage deviation [24], network losses, and voltage fluctuations [25], with lower-level models assessing the impact of configuration decisions and adjusting ESS operation accordingly. However, most prior studies focused on fundamental voltage deviation or a single power quality problem such as harmonic distortion and did not consider comprehensive mitigation across multiple power quality problems, thereby failing to fully exploit the potential of ESS to address multidimensional power quality challenges. More importantly, [15–17,21–25] overlooked the inherent power quality regulation capability of PV and its coordination with ESS, leading to underutilization of power quality control resources.

Beyond problem formulation, the selection of an appropriate solving algorithm plays a crucial role in ensuring the reliability and efficiency of ESS configuration results. For the upper-level ESS configuration model, it is typically formulated as a mixed-integer nonlinear programming (MINLP) problem. To tackle such complex optimization problems, [26] compared classical, analytical, and heuristic approaches, concluding that heuristic methods are the most suitable owing to their flexibility and adaptability, despite the lack of guaranteed global optimality. Building on this, recent studies have focused on improving existing heuristic methods or hybridizing them with other techniques [27,28]. For example, [29] enhanced the traditional genetic algorithm by incorporating linearized distribution power flow equations for rapid constraint verification, enabling fast and accurate ESS sizing. In hybrid algorithm research, [30] employed nondominated sorting genetic algorithm II (NSGA-II) to balance investment cost and economic return, and combined it with the cuckoo search algorithm to accelerate convergence. While the above methods enhance upper-level solution efficiency, the presence of numerous harmonic variables in power quality-aware ESS configuration makes the determination of optimal ESS siting and sizing a persistent challenge.

The lower-level ESS operational optimization is essentially an optimal power flow (OPF) problem. Since the nonlinearity and nonconvexity of OPF primarily stem from the power flow equations [31], many studies have focused on relaxing or approximating these equations using convex formulations. For instance, [32] employed a first-order Taylor expansion around a given operating point, combined with predicted power values and an enhanced semi-definite program relaxation to achieve linearization. Similarly, [33] linearized the power flow equations using a first-order Taylor expansion and discretized variables such as restoration switching sequences. In [34], the authors identified truncation errors and their first derivatives as key factors affecting linearization accuracy, and proposed constructing distinct linear models under different operating conditions. Reference [35] highlighted the inefficiency of nonlinear programming solvers and suggested linearizing the OPF model by incorporating elements such as resistance to represent power losses. It is worth noting that linearization methods based on first-order Taylor expansion are generally effective only under small perturbations. Since the ESS in this study is capable of harmonic compensation, the resulting OPF problem inherently involves high-frequency harmonic components and should be formulated as an optimal harmonic power flow (OHPF) problem. Under such conditions, traditional linearization techniques often fail to capture the nonlinearities introduced by harmonics, leading to significant inaccuracies.

1.3. Contribution and paper organization

In summary, configuring ESS in ADNs through bi-level optimization can effectively reduce power losses and enhance renewable energy integration. However, existing studies have predominantly focused on applications such as peak shaving, valley filling, and load curve smoothing, while paying limited attention to the potential of ESS in addressing power quality issues like harmonics and three-phase unbalance. Moreover, the synergistic effect of coordinated PV and ESS operation in power quality improvement remains largely unexplored, resulting in suboptimal economic returns from ESS deployment. To bridge these gaps, this paper proposes a bi-level optimization framework for ESS configuration that explicitly incorporates coordinated PV–ESS operation for power quality enhancement in ADNs. The main contributions are as follows:

1) To address the limited consideration of power quality in ESS configuration models, this paper proposes an enhanced bi-level optimization framework that explicitly incorporates power quality objectives. The upper level determines the optimal location and capacity of ESS, while the lower level establishes a multi-phase optimal harmonic power flow (MPOHPF) model to coordinate ESS and PV

outputs, aiming to minimize power loss and keep voltage deviations, harmonic distortions, and voltage unbalance within standard limits

2) To tackle the high-dimensional complexity of the upper-level ESS configuration model caused by the significant increase in harmonic variables, a candidate node selection method is proposed based on each node's mitigation potential. The method quantifies each node's contribution to deviations across multiple power quality metrics based on historical operating data, selects candidate nodes according to their overall impact, and solves the optimization problem using the improved grey wolf optimizer (IGWO) algorithm, thereby reducing the solution space and improving computational efficiency.
3) To overcome the nonlinearity and computational challenges of the lower-level MPOHPF model, power flow equations are reformulated using current injection models, and proper relaxation techniques are applied to convert the problem into a convex quadratically constrained quadratic program, enabling joint optimization of ESS and PV outputs. An alternating iterative algorithm between convex optimization process and power flow calculation is further employed to reduce approximation errors, and accommodate variations in nodal state variables. Compared to direct solving methods, the proposed method significantly enhances the efficiency of the computation process.

The remainder of the paper is structured as follows. The bi-level optimization model for ESS configuration with consideration of power quality enhancement is established in Section II. Section III details the solution approaches for both the upper and lower levels of the model. Section IV presents case study results and evaluates the economic performance of the proposed configuration model. Section V concludes this paper.

2. Optimization model establishment

This paper builds a bi-level optimization model for ESS configuration, incorporating comprehensive power quality improvement objectives. The entire optimization framework is shown in Fig. 1. The upper-level ESS configuration model is established based on economic optimality, taking into account the investment cost, operation and maintenance (OM) cost of ESS, the compensation cost for power quality improvement through the dispatch of existing PV, and the economic benefit resulting from enhanced power quality. In the lower-level optimization model, the MPOHPF model is established to compensate power quality in the ADN. The objective is to minimize power loss, subject to constraints on fundamental voltage magnitude, total harmonic distortion, and voltage unbalance.

2.1. Upper-level model

The investment in ESS typically includes investment, OM, and battery replacement costs [36]. This paper focuses on two key aspects: ESS configuration and power quality compensation. Accordingly, the installation and OM costs of ESS are considered as the initial investment. To address power quality compensation requirements, two cost indices are introduced: (1) the cost savings achieved through power quality improvement, measured by the reduction in power loss; (2) the compensation cost associated with utilizing PV to enhance power quality. These costs underpin the economic evaluation of ESS configuration and power quality improvement.

Objective function: 1) *Total investment cost minimization.*

The full lifecycle investment cost of the ESS is the sum of its installation cost, OM cost and battery degradation cost.

$$C_{LCC}^{E} = C_{inst}^{E} + C_{om}^{E} + C_{D}^{E} \tag{1}$$

The installation cost takes into account the power capacities of the ESS and its expected service life, as shown in (2). To ensure consistency in the time scale between the upper and lower levels of the bi-level model, the capital recovery factor (*CRF*) is used to annualize the ESS installation cost, as shown in (3).

$$C_{inst}^{E} = C_{inst,all}^{E} \cdot CRF = \left[\sum_{m=1}^{N_m}\left(C_{P,inst}P_{inst}^{E} + C_{E,inst}E_{inst}^{E}\right)\right]\cdot CRF \tag{2}$$

$$CRF = \frac{r(1+r)^{N_y}}{(1+r)^{N_y}-1} \tag{3}$$

where P_{E}^{inst} is the rated power of the configured ESS, and E_{E}^{inst} is its energy capacity. $C_{P,inst}$ is the unit cost per kW, and $C_{E,inst}$ is the unit cost per kWh. N_m is the number of ESS units configured, r is the discount rate, and N_y is the expected service life.

$$C_{om}^{E} = \left[\sum_{y=1}^{N_y}\frac{\sum_{m=1}^{N_m}\left(C_{P,om}P_{inst}^{E} + C_{E,om}E_{inst}^{E}\right)}{(1+r)^{y}}\right]\cdot CRF \tag{4}$$

where $C_{P,om}$ is the annual OM cost per kW, and $C_{E,om}$ is the annual cost per kWh of the ESS.

The ESS battery undergoes degradation during charge/discharge cycling. It is commonly assumed that the battery reaches end-of-life when its capacity declines to 80 % of the initial capacity. Therefore, the battery degradation cost of the ESS is calculated from the actual service life and the investment cost [37], as shown in (5). The actual service life and the number of battery replacements are determined by (6) and (7), respectively.

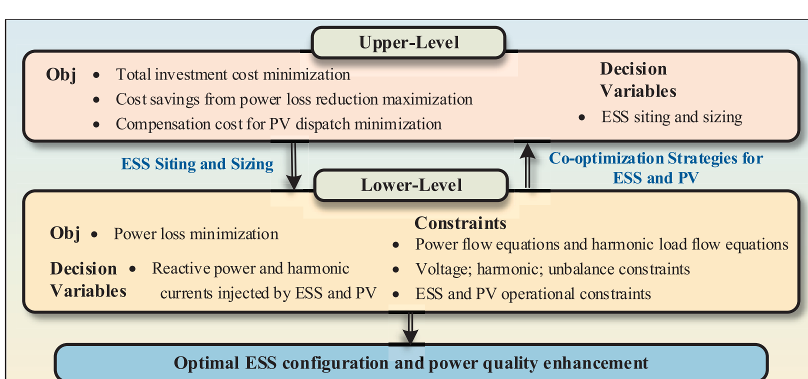

Fig. 1. Bi-level optimization framework.

$$C_D^E = \left(\sum_{i=1}^{N_d} \frac{C_r}{(1+r)^{(i \cdot N_a)}}\right) \cdot CRF \tag{5}$$

$$N_a = \frac{0.2 E_{inst}^E}{AG} \tag{6}$$

$$N_d = \lfloor \frac{N_y}{N_a} \rfloor \tag{7}$$

where C_r is the battery replacement cost, equal to the initial total ESS capacity cost. N_a is the actual service life. N_d is the number of battery replacements due to degradation. 0.2 represents the total capacity loss of the battery, and AG is the battery degradation rate.

2) *Cost savings from power loss reduction maximization.*

Configuring ESS effectively reduces network power loss. The resulting cost savings are incorporated into the objective function as an equivalent term.

$$C_{Loss} = \sum_{y=1}^{N_y} \sum_{t=1}^{d} P_{Loss}(t) Ce(t) \Delta t \tag{8}$$

where P_{Loss} is the active power loss at time t.

3) *Compensation cost for PV dispatch minimization.*

To maximize the utilization of PV and reduce the cost of ESS configuration, an economic compensation mechanism is introduced to transform distributed PV into a dispatchable asset for compensating harmonics, unbalance, and other power quality problems.

$$C_Q^{PV} = RPC \cdot \sum_{y=1}^{N_y} \sum_{t=1}^{d} S^{PV}(t) \Delta t \tag{9}$$

where RPC is the compensation cost coefficient for PV. $S^{PV}(t)$ is the dispatchable capacity of the distributed PV at time t, which includes the reactive power and harmonic current provided by the PV.

4) *Upper-level objective.*

The upper-level model, which takes the location and capacity of ESS as control variables, is nested with the lower-level model. It aims to minimize the ESS configuration cost, provided that the resulting configuration satisfies the power quality compensation requirements.

$$\min C_{all} = C_{LCC}^E + C_{Loss} + C_Q^{PV} \tag{10}$$

2.2. Lower-level model

In existing researches, OPF models primarily aim to minimize power loss, with constraints including fundamental power flow equations, voltage limits, and energy constraints of ESS charging and discharging. In this paper, the power quality control capabilities of both ESS and PV are considered by introducing harmonic distortion and voltage unbalance constraints to ensure that all power quality indices remain within acceptable ranges. Additionally, to ensure safe and stable system operation, harmonic power flow constraints and operational limits of ESS and PV inverters are incorporated.

Objective function: 1) *Minimization of power loss.*

Active power loss in the lines arises from both fundamental and harmonic current flows.

$$f_{loss} = \sum_{k=1}^{N_l} \sum_{h=1}^{H} \sum_{\varphi=a}^{n} P_{k,\varphi}^{loss,h} \tag{11}$$

where N_l is the total number of lines, and H specifies the highest harmonic order taken into account. The term $P_{k,\varphi}^{loss,h}$ represents the phase φ power loss of line k at harmonic order h, which is calculated as the difference in active power between the two terminals of the component, as shown in (12).

$$P_{k,\varphi}^{loss,h} = real\left[\sum_{\varphi'=a}^{n} y_{k,\varphi,\varphi'}^{h} \left(\dot{U}_{i,\varphi}^{h} - \dot{U}_{j,\varphi}^{h}\right)\left(\dot{U}_{i,\varphi'}^{h} - \dot{U}_{j,\varphi'}^{h}\right)^{*}\right] \tag{12}$$

where $y_{k,\varphi',\varphi}^{h}$ corresponds to the h-th harmonic admittance between phase φ and φ' of line k, and $\dot{U}_{i,\varphi}^{h}$ indicates the harmonic voltage phasor at phase φ of node i. The symbol * indicates the complex conjugate.

2) *Objective of MPOHPF.*

$$\min f = \frac{f_{loss}}{F_{loss}} \tag{13}$$

where F_{loss} denotes the baseline value of the objective function prior to compensation.

As shown in (11) and (12), f is a quadratic function of node voltages, and satisfies $f_{loss} \geqslant 0$, indicating that it is a convex quadratic function with respect to the voltage variables.

Constraint: 1) *Power flow equation constraints.*

$$\begin{aligned} P_{i,\varphi\varphi'}^{PV} + jQ_{i,\varphi\varphi'}^{PV} &= (\dot{U}_{i,\varphi}^{1} - \dot{U}_{i,\varphi'}^{1})(\dot{I}_{i,\varphi\varphi'}^{PV1})^{*} \\ P_{i,\varphi\varphi'}^{L} + jQ_{i,\varphi\varphi'}^{L} &= (\dot{U}_{i,\varphi}^{1} - \dot{U}_{i,\varphi'}^{1})(\dot{I}_{i,\varphi\varphi'}^{L1})^{*} \\ P_{i,\varphi\varphi'}^{E} + jQ_{i,\varphi\varphi'}^{E} &= (\dot{U}_{i,\varphi}^{1} - \dot{U}_{i,\varphi'}^{1})(\dot{I}_{i,\varphi\varphi'}^{E1})^{*} \end{aligned} \tag{14}$$

where the superscripts PV, L and E denote that the associated variables correspond to the PV, load and ESS, respectively. $P_{i,\varphi\varphi'}^{E}$ and $Q_{i,\varphi\varphi'}^{E}$ indicate the active and reactive power contributions from the ESS linked between phases φ and φ' at node i.

2) *Harmonic load flow equation constraints.*

The harmonic loads in the ADNs are commonly modeled as current sources [38], with their injected harmonic currents computed using (15).

$$\begin{aligned} \left|\dot{I}^{h}\right| &= \left|\dot{I}^{1}\right| \frac{I_{h-spectrum}}{I_{1-spectrum}} \\ \theta_h &= \theta_{h-spectrum} + h(\theta_1 - \theta_{1-spectrum}) \end{aligned} \tag{15}$$

where the harmonic and fundamental current magnitudes generated by the loads are denoted by $|\dot{I}^{h}|$ and $|\dot{I}^{1}|$, respectively, and the phase angle of the phasor enclosed in the bracket is indicated by θ_h. $I_{h-spectrum}$ and $\theta_{h-spectrum}$ correspond to the amplitude and phase spectra of the harmonic currents.

The relationship between the h-*th* harmonic current injected at node i and the corresponding h-*th* harmonic voltage forms the harmonic power flow constraint, as shown in (16).

$$\dot{I}_{i,\varphi}^{h} = \sum_{\varphi' \neq \varphi} (\dot{I}_{i,\varphi\varphi'}^{Lh} + \dot{I}_{i,\varphi\varphi'}^{Eh}) = \sum_{j=1}^{N_n} \sum_{\varphi'=a}^{n} (y_{i,\varphi,j,\varphi'}^{h} \dot{U}_{j,\varphi'}^{h}) \tag{16}$$

3) *Voltage constraints.*

The constraint defined in (17) specifies the permissible range for the fundamental voltage magnitude.

$$U_{\min} \leqslant \left|\dot{U}_{i,\varphi}^{1}\right| \leqslant U_{\max} \tag{17}$$

where $U_{\min}$ and $U_{\max}$ are the lower and upper bounds

4) *Harmonic constraints.*

The harmonic constraint in (18) specifies the allowable limit of total harmonic distortion at each node.

$$\sum_{h=3}^{H} \left|\dot{U}_{i,\varphi}^{h}\right|^{2} \leqslant (U_{\max}^{h})^{2} \tag{18}$$

where $U_{\max}^{h}$ is the upper bound.

5) *Voltage unbalance constraints.*

The unbalance constraint in (19) defines the permissible voltage unbalance at each node.

$$\left|\frac{(\dot{U}_{i,a}^{1}+e^{j240^{\circ}}\dot{U}_{i,b}^{1}+e^{j120^{\circ}}\dot{U}_{i,c}^{1})}{(\dot{U}_{i,a}^{1}+e^{j120^{\circ}}\dot{U}_{i,b}^{1}+e^{j240^{\circ}}\dot{U}_{i,c}^{1})}\right|^{2}\leqslant(U_{\max}^{u})^{2} \tag{19}$$

where $U_{\max}^{u}$ is the upper bound.

6) *Maximum charging power constraint of the ESS.*

$$-P_{\max}\leqslant P_{t,i,\varphi\varphi'}^{E}\leqslant P_{\max} \tag{20}$$

where $P_{t,i,\varphi\varphi'}^{E}$ is the ESS power at time t, and $P_{\max}$ is its rated active power. $-P_{\max}$ indicates discharging.

7) *Charging and discharging capacity constraint of the ESS.*

$$E_{\min}\leqslant\int_{0}^{T}P_{i,\varphi\varphi'}^{E}(t)\leqslant E_{\max} \tag{21}$$

where $E_{\min}$ and $E_{\max}$ denote the lower and upper limits, respectively.

8) *Inverter capacity limits for ESS and PV.*

The reactive power and harmonic current outputs of ESS and PV are limited by the rated capacities of their grid-connected inverters, as formulated in (22) and (23).

$$\left(\sum_{h=1}^{H}\left|\dot{U}_{i,\varphi}^{h}-\dot{U}_{i,\varphi'}^{h}\right|^{2}\right)\left(\sum_{h=1}^{H}\left|\dot{I}_{i,\varphi\varphi'}^{Eh,PVh}\right|^{2}\right)\leqslant(S_{\max})^{2} \tag{22}$$

$$\sum_{h=1}^{H}\left|\dot{I}_{i,\varphi\varphi'}^{Eh,PVh}\right|^{2}\leqslant(I_{\max})^{2} \tag{23}$$

where $S_{\max}$ is its rated active power, and $I_{\max}$ is its rated active power.

Due to the existence of nonlinear equality constraints (14) and nonconvex inequality constraints (17), (19), (21), (22), the established OHPF problem is both nonconvex and nonlinear. The control variables of the model are the harmonic currents and reactive power outputs of the ESS and PV systems.

3. Model-solving method

3.1. Upper-level model solving

The introduction of harmonic and voltage unbalance constraints necessitates the inclusion of harmonic components (e.g., 3rd, 5th, and 7th orders) in the optimization model, significantly increasing its dimensionality. To address this challenge, a promising strategy is to narrow the configuration scope-i.e., pre-select a limited set of candidate nodes for ESS siting before optimization. For this purpose, this section proposes a candidate node selection method based on power quality contributions. The IGWO algorithm offers strong global search capability and maintains population diversity via an adaptive mechanism, thereby reducing the risk of trapping in local optima and achieving a favorable balance between solution quality and computational efficiency [3940]. Accordingly, the IGWO algorithm is employed to identify optimal location and capacity for ESS configuration.

Candidate node selection: 1) *Voltage deviation contribution.*

In the radial distribution network shown in Fig. 2, the power at node i is $P_{i,\varphi}+jQ_{i,\varphi}$, the injected power from the PV is $P_{PV,\varphi}+jQ_{PV,\varphi}$, and the impedance between nodes i-1 and i is $R_{i-1,\varphi,i,\varphi'}^{1}+jX_{i-1,\varphi,i,\varphi'}^{1}$. The fundamental voltage at each node $U_{i,\varphi'}^{1}$ is derived based on the voltage drop theory, as expressed in (24).

$$U_{i,\varphi}^{1}=U_{0,\varphi}^{1}-\sum_{j=1}^{i}\frac{\sum_{k=j}^{N_n}\sum_{\varphi'\neq\varphi}\left(P_{k,\varphi}r_{i,\varphi,j,\varphi'}^{1}+Q_{k,\varphi}x_{i,\varphi,j,\varphi'}^{1}\right)}{U_{0,\varphi}^{1}} \tag{24}$$

After calculating fundamental power flow, the fundamental currents of loads and PV systems $I_{j,\varphi\varphi'}^{1}$ can be obtained. These current values are used to replace the original PQ nodes in the distribution network. When the feeder source node is a balanced node, the voltage deviation Dev_i relative to the reference voltage is defined, as shown in (25).

$$Dev_{i}=\sum_{j=1}^{n}\mathbf{Z}_{i,\varphi,j,\varphi'}\dot{I}_{j,\varphi\varphi'}^{1} \tag{25}$$

where $\mathbf{Z}_{i,\varphi,j,\varphi'}$ is the nodal impedance matrix, $\mathbf{Z}_{i,\varphi,j,\varphi'}=R_{i,\varphi,j,\varphi'}+jX_{i,\varphi,j,\varphi'}$. The relative contribution of node j to the voltage deviation at node i is defined as shown in (26).

$$C_{j-i}^{1}=\frac{\left|\mathbf{Z}_{i,\varphi,j,\varphi'}I_{j,\varphi\varphi'}^{1}\right|}{|Dev_{i}|} \tag{26}$$

Based on (26), the cumulative contribution sources of node i can be calculated. Accordingly, a binary 0–1 matrix representing the contribution relationship from node j to node i is defined, as shown in (27).

$$\begin{aligned}&M_{j-i}^{1}=I(\textstyle\sum_{S_i}C_{j-i}^{1}\geqslant\tau)\\&S_{i}^{1}=\left\{j\in\{1,2,\ldots,n\}\middle|\textstyle\sum_{k\in S_i}C_{j-i}^{1}\geqslant\tau\right\}\end{aligned} \tag{27}$$

where $I(\cdot)$ is an index function that equals 1 when the condition is satisfied; S_i^1 is the set of cumulative contribution sources; and τ is the cumulative contribution threshold.

2) *Harmonic distortion contribution.*

For harmonics, after calculating harmonic power flow and obtaining the harmonic current $\dot{I}_{j,\varphi\varphi'}^{h}$ at each node, the harmonic voltage distortion $U_{i,\varphi}^{h}$ is defined, as shown in (28).

$$Dis_{i}=\sum_{j=1}^{n}\mathbf{Z}_{i,\varphi,j,\varphi'}^{h}\dot{I}_{j,\varphi\varphi'}^{h} \tag{28}$$

where $\mathbf{Z}_{i,\varphi,j,\varphi'}^{h}$ is the nodal harmonic impedance matrix.

The relative contribution of harmonic source node j to the harmonic voltage distortion at other nodes is defined, as shown in (29).

$$C_{j-i}^{h}=\frac{\left|\mathbf{Z}_{i,\varphi,j,\varphi'}^{h}I_{j,\varphi\varphi'}^{h}\right|}{|Dis_{i}|} \tag{29}$$

By extending (27), the cumulative contribution source matrix M_{j-i}^{h} and the cumulative contribution source set S_i^h for harmonic voltage distortion at each node are established.

3) *Voltage unbalance contribution.*

Voltage unbalance is primarily caused by unequal loading among the

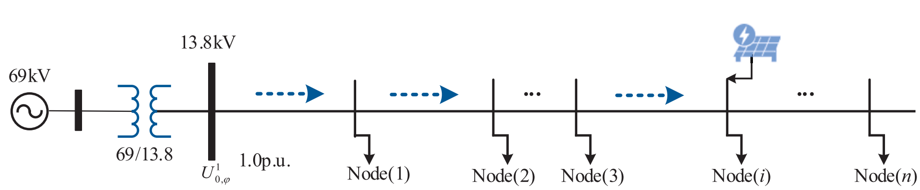

Fig. 2. Radial distribution network.

three phases. Using the symmetrical component transformation matrix **T** in (30), the unbalanced fundamental voltage can be decomposed into positive, negative, and zero-sequence components. The negative-sequence voltage is used to reflect the degree of asymmetry in the system.

$$\mathbf{T} = \frac{1}{3}\begin{bmatrix} 1 & 1 & 1 \\ 1 & a^2 & a \\ 1 & a & a^2 \end{bmatrix}, a = e^{j120^\circ} \tag{30}$$

By mapping the three-phase impedance, voltage, and current into the sequence component coordinate system, the sequence impedance matrix $Z^{012}_{i,\varphi,j,\varphi'}$, negative-sequence voltage $U^1_{2,i}$, and negative-sequence current $I^1_{2,i}$ are obtained, as shown in (31). The voltage unbalance at each node is then defined as shown in (32).

$$\begin{cases} Z^1_{012,i,j} = \boldsymbol{T} \cdot Z^1_{i,\varphi,j,\varphi'} \cdot \mathbf{T}^{-1} \\ U^1_{2,i} = \frac{1}{3}\left(U^1_{i,a} + a^2 U^1_{i,b} + a U^1_{i,c}\right) \\ I^1_{2,i} = \frac{1}{3}\left(I^1_{i,a} + a^2 I^1_{i,b} + a I^1_{i,c}\right) \end{cases} \tag{31}$$

$$Neg_i = \sum_{j=1}^{n} Z^1_{2,i,j} I^1_{2,i} \tag{32}$$

where, negative-sequence impedance matrix is $Z^1_{2,i,j}$, and $Z^1_{2,i,j} = \left[Z^1_{012,i,j}\right]_{22}$.

The relative contribution C^2_{j-i} of node j to the voltage unbalance Neg_i at node i is shown in (33).

$$C^2_{j-i} = \frac{\left|Z^1_{2,i,j} I^1_{2,i}\right|}{|Neg_i|} \tag{33}$$

By extending (27), the cumulative contribution source matrix M^2_{j-i} and the cumulative contribution source set S^2_i for voltage unbalance at each node are established.

4) *Aggregated contribution source set.*

Since different nodes in the ADNs are affected by different power quality issues, the contribution source sets with significant impact on fundamental voltage deviation S^1_i, harmonic voltage distortion S^h_i, and negative-sequence voltage S^2_i are combined through set union, as shown in (34), to identify key candidate nodes for power quality compensation.

$$S_i = S^1_i \cup S^h_i \cup S^2_i \tag{34}$$

Solving procedure:

*Step*1: Based on the nodal impedance matrix $Z_{i,\varphi,j,\varphi'}$, harmonic impedance matrix $Z^h_{i,\varphi,j,\varphi'}$, the active and reactive power of all nodes, and the harmonic model established in (15), both fundamental and harmonic power flow calculations are carried out. As a result, the fundamental currents I^{L1}, I^{PV1}, and the harmonic currents I^{Lh} are obtained.

*Step*2: Application of a contribution calculation framework for various power quality problems:

- For fundamental voltage deviation: Based on (24)-(26), the voltage deviation Dev_i and its mapping to each node's fundamental voltage contribution C^1_{j-i} are calculated;
- For harmonic voltage distortion: Based on (28)-(29), the harmonic distortion Dis_i and its mapping to each node's harmonic voltage contribution C^h_{j-i} are calculated;
- For voltage unbalance: Based on (32)-(33), the voltage unbalance Neg_i and its mapping to each node's contribution to voltage unbalance C^2_{j-i} are calculated.

*Step*3: Based on C^1_{j-i}, C^h_{j-i}, and C^2_{j-i}, the binary contribution matrices M^1_{j-i}, M^h_{j-i}, and M^2_{j-i} are constructed, and the corresponding contribution source sets S^1_i, S^h_i, and S^2_i for each power quality indices are identified.

*Step*4: By repeatedly performing *Step*2 and *Step*3 on historical operating data and calculating the cumulative power quality contribution matrix, contribution source sets S^1_i, S^h_i, and S^2_i are updated at a 95 % confidence level. Then, the unified aggregated contribution source set S_i is selected according to (34).

*Step*5: The set S_i is used as the solution space for the IGWO algorithm to iteratively solve the upper-level model. In each iteration, the total investment cost is calculated according to (10), until the optimal ESS location and capacity are obtained.

3.2. Lower-level model solving

As the MPOHPF model considers power quality, multiple constraints and optimization variables related to both fundamental and harmonic power flows are involved. As a result, traditional DC-linear models and power flow linearization methods based on first-order Taylor expansion become inaccurate. Therefore, convexification is required during the solution process. In this paper, power flow equations are replaced with current injection equations, and several relaxation techniques are adopted, thereby transforming the model into a convex quadratically constrained quadratic program problem. To eliminate trigonometric functions related to phase angles, complex quantities are represented in rectangular form, as shown in (35).

$$\begin{aligned} \dot{U}^h_{i,\varphi} &= U^h_{i,\varphi,x} + \mathrm{j}U^h_{i,\varphi,y} \\ \dot{I}^h_{i,\varphi\varphi'} &= I^h_{i,\varphi\varphi',x} + \mathrm{j}I^h_{i,\varphi\varphi',y} \\ y^h_{i,\varphi,j,\varphi'} &= g^h_{i,\varphi,j,\varphi'} + \mathrm{j}b^h_{i,\varphi,j,\varphi'} \end{aligned} \tag{35}$$

where the subscripts x and y denote the real and imaginary components of voltage and current phasors, respectively, while g and b correspond to the conductance and susceptance of elements within the nodal admittance matrix. To eliminate the nonlinear equality constraints, power flow and harmonic load flow analyses are first performed. This yields the initial values of both fundamental and harmonic currents for subsequent optimization. The power flow equations can then be simplified, as shown in (36).

$$\begin{aligned} \sum_{\varphi'\neq\varphi}\left(I^{L1(0)}_{i,\varphi\varphi',x} + I^{PV1(0)}_{i,\varphi\varphi',x}\right) &= \sum_{j=1}^{N_n}\sum_{\varphi'=a}^{n}\left(g^1_{i,\varphi,j,\varphi'}U^1_{j,\varphi',x} - b^1_{i,\varphi,j,\varphi'}U^1_{j,\varphi',y}\right) \\ \sum_{\varphi'\neq\varphi}\left(I^{L1(0)}_{i,\varphi\varphi',y} + I^{PV1(0)}_{i,\varphi\varphi',y}\right) &= \sum_{j=1}^{N_n}\sum_{\varphi'=a}^{n}\left(g^1_{i,\varphi,j,\varphi'}U^1_{j,\varphi',y} + b^1_{i,\varphi,j,\varphi'}U^1_{j,\varphi',x}\right) \\ \sum_{\varphi'\neq\varphi}\left(I^{Lh(0)}_{i,\varphi\varphi',x}\right) &= \sum_{j=1}^{N_n}\sum_{\varphi'=a}^{n}\left(g^h_{i,\varphi,j,\varphi'}U^h_{j,\varphi',x} - b^h_{i,\varphi,j,\varphi'}U^h_{j,\varphi',y}\right) \\ \sum_{\varphi'\neq\varphi}\left(I^{Lh(0)}_{i,\varphi\varphi',y}\right) &= \sum_{j=1}^{N_n}\sum_{\varphi'=a}^{n}\left(g^h_{i,\varphi,j,\varphi'}U^h_{j,\varphi',y} + b^h_{i,\varphi,j,\varphi'}U^h_{j,\varphi',x}\right) \end{aligned} \tag{36}$$

where the superscript (0) denotes the initial value before optimization.

After replacing the nonlinear power flow constraints using (36), the control variables $Q^G_{i,\varphi\varphi'}$ in the MPOHPF model is replaced by $I^{E1}_{i,\varphi\varphi',x}$, $I^{E1}_{i,\varphi\varphi',y}$, $I^{Eh}_{i,\varphi\varphi',x}$, and $I^{Eh}_{i,\varphi\varphi',y}$ here. The energy exchanged (charged/discharged) by the ESS must not exceed its energy capacity, as constrained by (37).

$$E_{\min} \leqslant \int_0^T \left(U^{1(0)}_{i,\varphi,x} - U^{1(0)}_{i,\varphi',x}\right)I^{E1}_{i,\varphi\varphi',x}(t) + \left(U^{1(0)}_{i,\varphi,y} - U^{1(0)}_{i,\varphi',y}\right)I^{E1}_{i,\varphi\varphi',y}(t) \leqslant E_{\max} \tag{37}$$

It is approximately assumed that the active power output of the ESS remains constant during the 15-minute dispatch interval. Therefore, the approximation in (38) is used to replace (37).

$$\begin{cases} E^t - P_{t+1} \times 0.25 \geqslant E_{\min} \\ E^t + P_{t+1} \times 0.25 \leqslant E_{\max} \end{cases} \tag{38}$$

where E^t is the total energy stored in the ESS at time t, and P_{t+1} is the active power output of the ESS in the $(t+1)$ time period. The coefficient 0.25 represents the time interval of 15 min, converted into hours. It is used to calculate the energy variation of the ESS within each dispatch period as the product of power and time.

To ensure the economic benefits of PV users, active power generation must be prioritized for PV output, and constraint (39) is subsequently introduced.

$$(U^{1(0)}_{i,\varphi,x} - U^{1(0)}_{i,\varphi',x})I^{PV1}_{i,\varphi\varphi',x} + (U^{1(0)}_{i,\varphi,y} - U^{1(0)}_{i,\varphi',y})I^{PV1}_{i,\varphi\varphi',y} = P^{PV}_{i,\varphi\varphi'} \tag{39}$$

In addition, the inverter constraints (22)-(23) are reformulated into a convex representation, as shown in (40) and (41).

$$\sum_{h=1}^{H}\left(\left(U^{h(0)}_{i,\varphi,x} - U^{h(0)}_{i,\varphi',x}\right)^2 + \left(U^{h(0)}_{i,\varphi,y} - U^{h(0)}_{i,\varphi',y}\right)^2\right) \times \sum_{h=1}^{H}\left(\left(I^{Eh/PVh}_{i,\varphi\varphi',x}\right)^2 + \left(I^{Eh/PVh}_{i,\varphi\varphi',y}\right)^2\right) \leqslant (S_{\max})^2 \tag{40}$$

$$\sum_{h=1}^{H}\left(\left(I^{Eh/PVh}_{i,\varphi\varphi',x}\right)^2 + \left(I^{Eh/PVh}_{i,\varphi\varphi',y}\right)^2\right) \leqslant (I_{\max})^2 \tag{41}$$

Given that the fundamental positive-sequence voltage typically dominates over both the negative-sequence and harmonic components, voltage unbalance can be approximately characterized by the magnitude of the negative-sequence voltage, while harmonic distortion is assumed to be proportional to the corresponding harmonic voltage amplitude. Accordingly, constraints (42) and (43) are employed as convex alternatives to (18) and (19) to preserve the convexity of the problem.

$$\sum_{h=1}^{H}\left(\left(U^{h}_{i,\varphi,x}\right)^2 + \left(U^{h}_{i,\varphi,y}\right)^2\right) \leqslant \left(U^{h}_{\max}\right)^2 \tag{42}$$

$$\left(U^1_{i,a,x} - \frac{1}{2}U^1_{i,b,x} - \frac{1}{2}U^1_{i,c,x} + \frac{\sqrt{3}}{2}U^1_{i,b,y} - \frac{\sqrt{3}}{2}U^1_{i,c,y}\right)^2 + \left(U^1_{i,a,y} - \frac{\sqrt{3}}{2}U^1_{i,b,x} + \frac{\sqrt{3}}{2}U^1_{i,c,x} - \frac{1}{2}U^1_{i,b,y} - \frac{1}{2}U^1_{i,c,y}\right)^2 \leqslant 9\left(U^u_{\max}\right)^2 \tag{43}$$

where $U^h_{\max}$ and $U^u_{\max}$ are the upper bounds of harmonics and voltage unbalance.

As shown in Fig. 3, voltage constraints are represented in rectangular coordinates. Given that phase angle variations at each node in the ADN are typically limited, the voltage feasibility region can be approximated by a trapezoidal area, highlighted by the shaded region in Fig. 3(a). Accordingly, the voltage constraint for each phase can be transformed into a group of linear inequalities. Taking phase b as an example, the corresponding constraints are expressed in (44).

$$\begin{aligned} &-2\sqrt{3}\overline{U} \leqslant (3U^1_{i,b,y} + \sqrt{3}U^1_{i,b,x}) \leqslant -2\sqrt{3}\underline{U} \\ &U^1_{i,b,y} - \tan(240^\circ - \delta/2)U^1_{i,b,x} \leqslant 0 \\ &U^1_{i,b,y} - \tan(240^\circ + \delta/2)U^1_{i,b,x} \geqslant 0 \end{aligned} \tag{44}$$

where δ denotes the allowable variation in the phase angle. The approximation accuracy is governed by δ and deteriorates as δ increases. This study adopts $\delta = 10^\circ$, which covers voltage phase angle deviations in most distribution networks, with a maximum absolute error of 0.0038 $\overline{U}$, as shown in Fig. 3(b).

After an initial power flow calculation at the current time step, all nodes are treated as constant current sources. However, once the ESS is configured and coordinated with PV for system optimization, the power flow will change. The accuracy of this approximation method is largely influenced by the initial power flow calculation results. Therefore, to eliminate approximation errors, this paper adopts an alternating iterative method between power flow calculation and optimization. In this approach, the output of the power flow calculation serves as the input for the optimization, and vice versa. The process repeats until the results converge with no significant variation.

In summary, the solution process of the lower-level MPOHPF model is shown in Fig. 4.

3.3. Overall process of the optimization procedure

The overall flowchart of the bi-level optimization model is shown in Fig. 5. In the upper-level, after candidate node selection, the ESS location is chosen from the candidate set, and its installation capacity is optimized as a continuous variable. Given the resulting location and capacity, the lower-level solves an OHPF problem with the objectives of minimizing active power loss and optimizing power quality. The lower-level results are then returned to the upper-level. If the lower-level fails to converge or violates constraints, a large penalty is imposed in the upper-level objective to steer the search away from the current configuration. The procedure repeats until convergence, yielding the optimal configuration and operation.

4. Case study

4.1. 162-node test network

The proposed method is validated on a 162-node three-phase four-

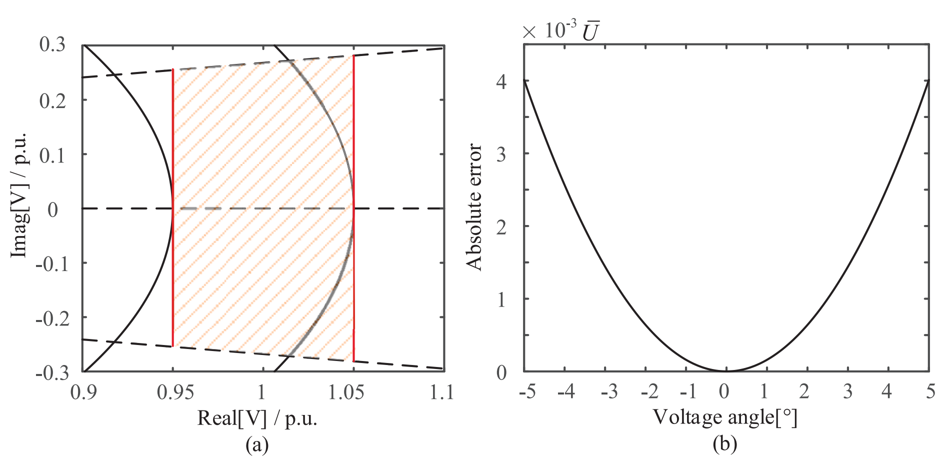

Fig. 3. Relaxed representation of voltage constraint.

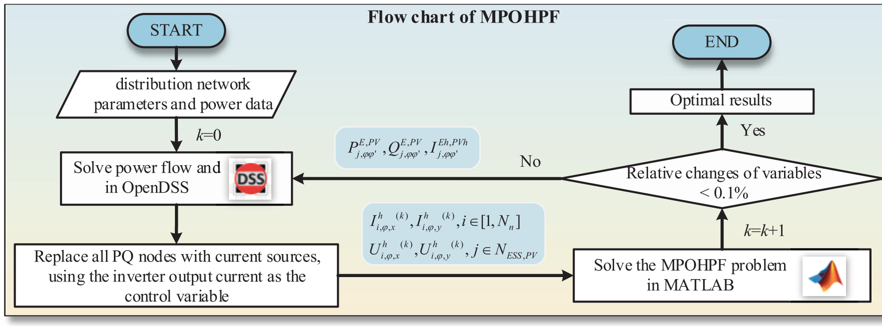

Fig. 4. Flow chart of MPOHPF.

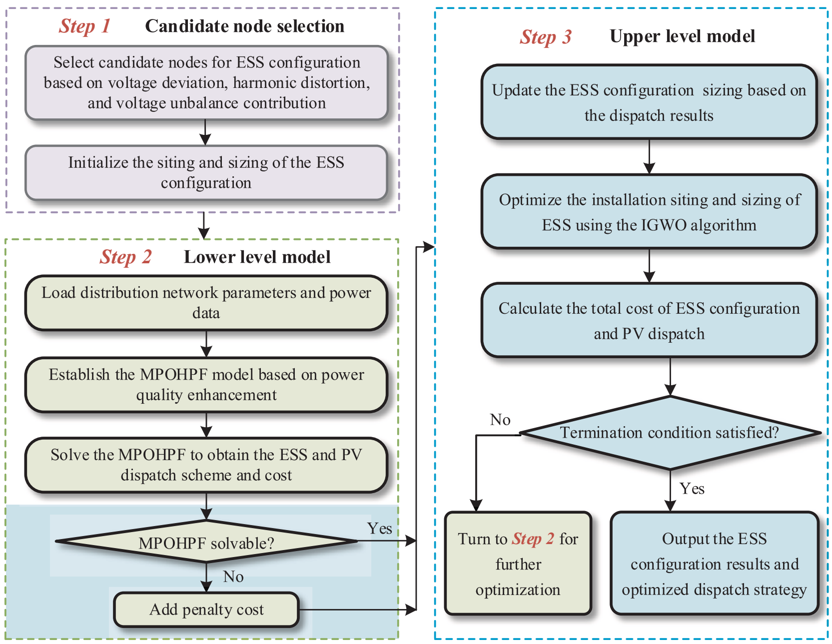

Fig. 5. Flow chart of the bi-level optimization model.

wire distribution network. The topology, load types, and line types of the test system are shown in Fig. 6, with detailed network parameters provided in [41].

In this case study, predefined 15-minute interval profiles of active and reactive power are adopted to replicate smart meter data at each node, including residential, commercial, and industrial loads. To ensure user generation benefits, PV power profiles are determined based on the maximum power point tracking. The locations and total installed capacities of PV units and different types of loads are shown in Fig. 6 and Fig. 7. Detailed information regarding the load nodes and PV connection points is summarized in Table 1. Harmonic orders 3, 5, 7, and 9 are considered, with their spectral characteristics derived from [42].

The basic configuration details of ESS [43,44] and the compensation cost coefficient for PV are presented in Table 2. The time-of-use (TOU) electricity pricing data, sourced from [45], are shown in Fig. 8.

4.2. Verification of the candidate node selection

Based on the candidate node selection process described in Section 3.1.2, the distributions of contribution sources for fundamental voltage deviation, harmonic voltage distortion, and voltage unbalance are shown in Fig. 9. As shown in the figure, the contribution sources of harmonic voltage distortion exhibit a clear clustering pattern, primarily concentrated at a few load nodes with high power levels and significant harmonic spectra. In contrast, the contribution sources of fundamental voltage deviation are more widely distributed and partially overlap with those of harmonic distortion. The sources contributing to voltage unbalance are mainly associated with a large number of single-phase loads that are widely distributed throughout the system, making them the most numerous and broadly dispersed. Therefore, by comprehensively considering the contributions of fundamental voltage deviation, harmonic distortion, and voltage unbalance, a total of 20 candidate nodes are selected, as listed in Table 3.

Fig. 10 presents a comparison between the convergence curves of the configuration problem addressed by IGWO with and without candidate node selection. It can be observed that the node selection process notably enhances the computational efficiency of the bi-level model, resulting in an approximately 70 % reduction in the average number of iterations. In addition, the proposed approach achieves superior solution accuracy.

4.3. ESS configuration results

After solving the bi-level optimization model, the locations and capacities of the ESS configuration in the 162-node network are presented in Table 4. Among the nodes with ESS configurations, the harmonic current, total current (including all fundamental and harmonic components), and reactive power output by the ESS at node 80 are shown in

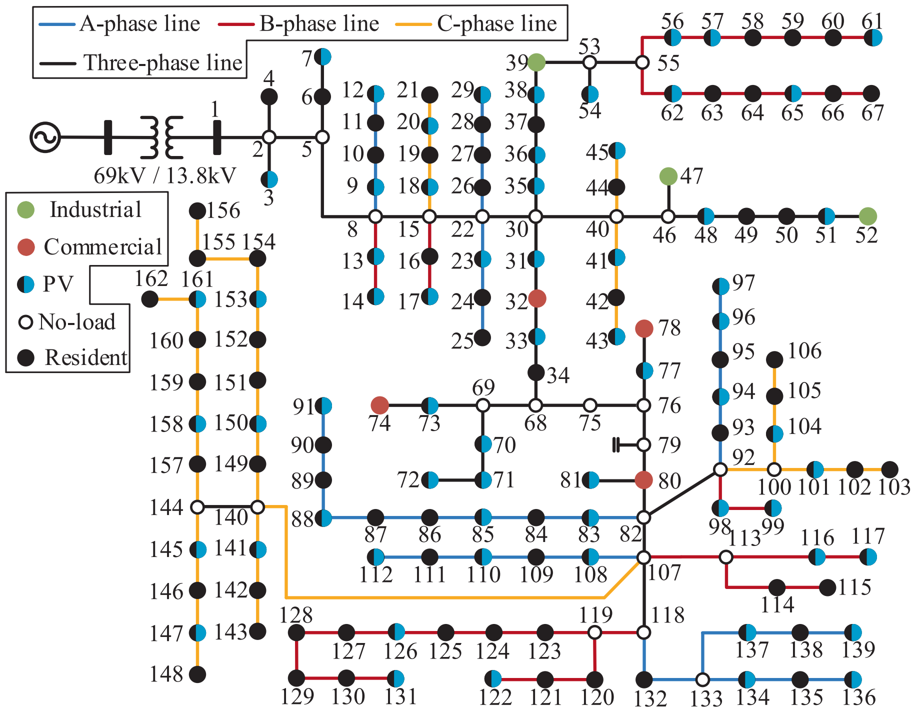

Fig. 6. 162-node distribution network.

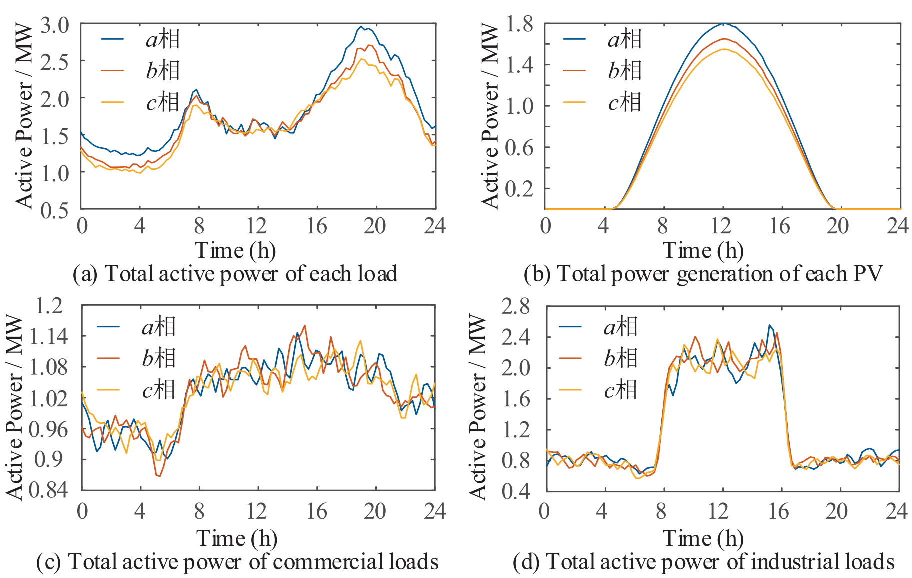

Fig. 7. Basic information on loads.

Table 1
Fundamental characteristics of the 162-node test system.

Load node number	phase a/b/c: 65/62/64
Peak residential load	2.96/2.71/2.52 MW, power factor: 0.95
PV number	36/33/31 per phase
Every PV peak generation	50 kW per phase
PV penetration rate (PV peak generation/ Peak load)	60 %/60 %/61.5 %

Table 2
The basic information of ESS.

Expected service life (N_y)	15 (year)
Actual service life (N_a)	9 (years)
Discount rate (r)	6 %
Cost per unit of power capacity	405.56 ($/kW)
Cost per unit of energy capacity	225.06 ($/kWh)
OM cost of power	1 % ($/year)
OM cost of energy	10 ($/kWh/year)
Compensation cost coefficient (RPC)	1.5 % of the TOU

Fig. 11 (a), (b), and (c), respectively. The harmonic current, total current, and reactive power output of all PVs in the network are shown in Fig. 11 (d), (e), and (f), respectively. It can be observed that between

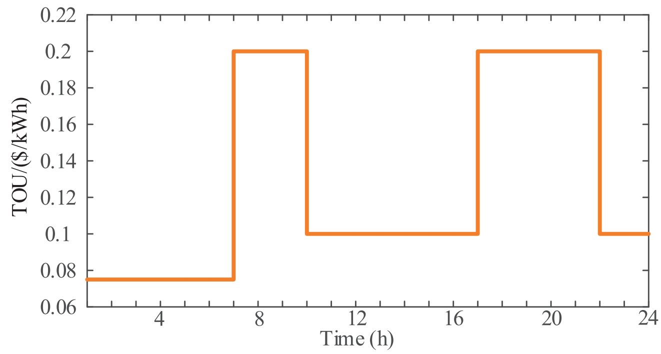

Fig. 8. Time of use electricity price for one day.

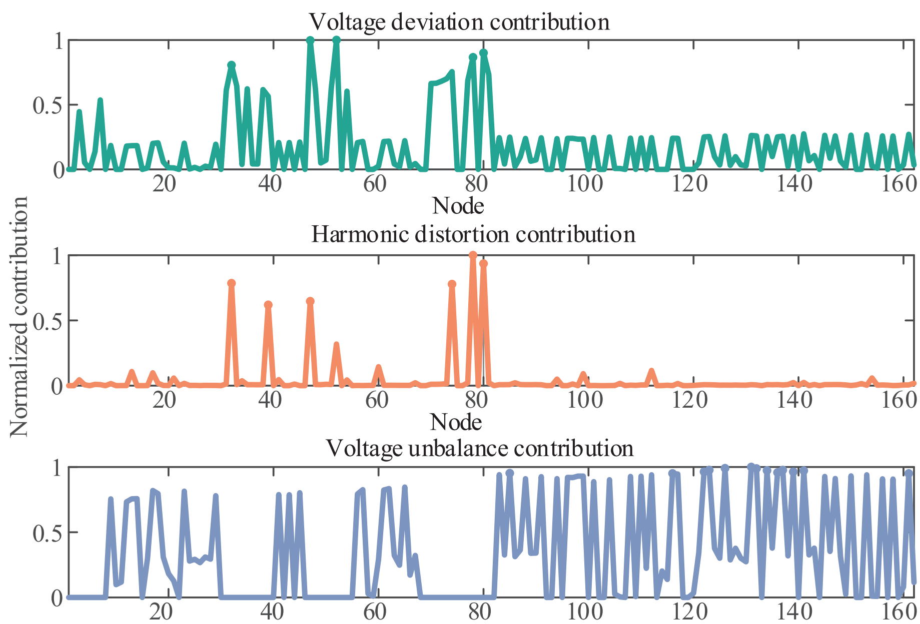

Fig. 9. Power quality contribution source distribution

Table 3
The candidate node of ESS.

Three-phase node	Phase A node	Phase B node	Phase C node
32, 39, 47, 52, 74, 78, 80	85, 132, 134, 136, 137, 139	116, 122, 123, 126, 131	141, 161

Table 4
The configuration result of ESS-PV.

Bus 32	350 kW/Phase	Bus 52	450 kW/Phase
Bus 80	550 kW/Phase	Bus 123	150 kW/Phase
Bus 136	350 kW/Phase	Bus 161	150 kW/Phase

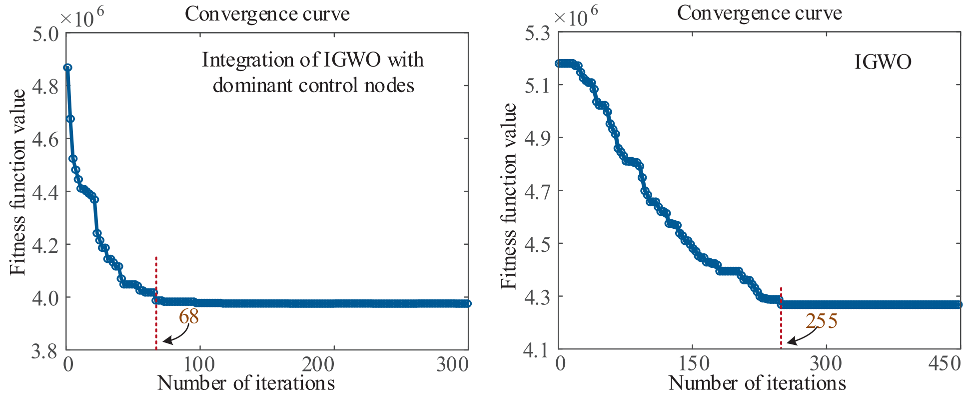

Fig. 10. Convergence curve of the upper-level optimization model.

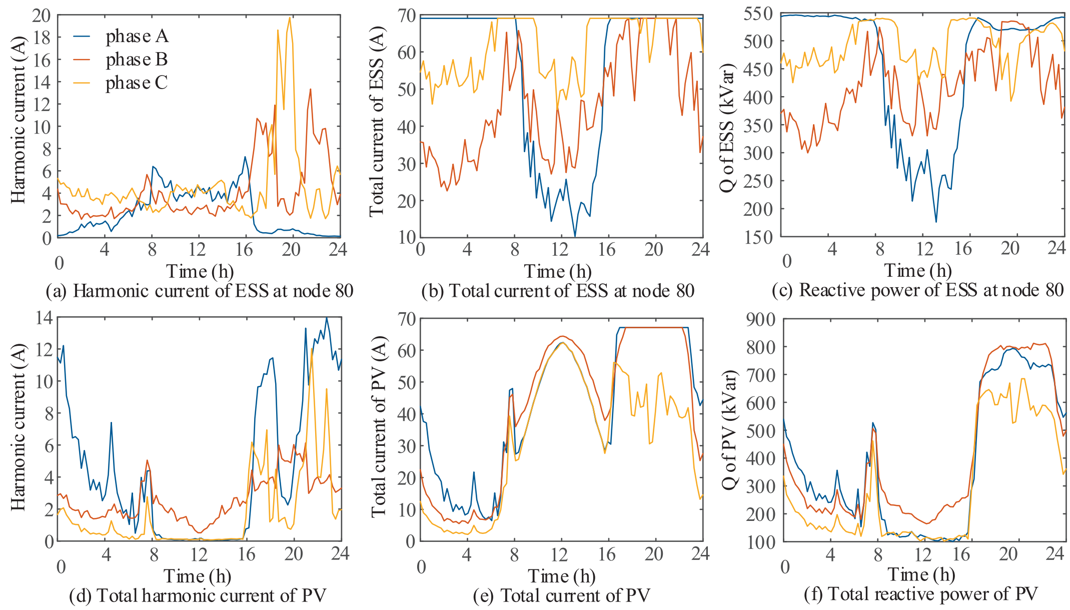

Fig. 11. Partial output results of ESS and PV.

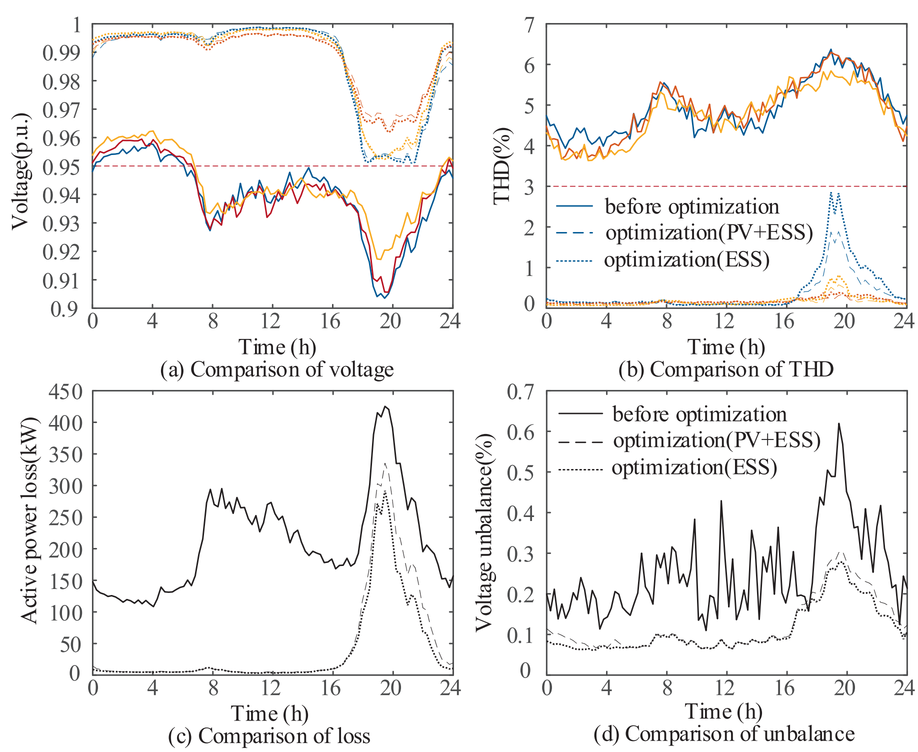

Fig. 12. Comparison of power quality before and after optimization

0–8 h and 16–24 h, the output currents of both the ESS and PV are limited by the inverter capacity. Additionally, the PV system generates a significant amount of current and reactive power during the nighttime, providing additional support for the high-quality power supply requirements.

Table 5
Case B.

Bus 32	450 kW/Phase	Bus 52	550 kW/Phase
Bus 80	550 kW/Phase	Bus 123	350 kW/Phase
Bus 136	450 kW/Phase	Bus 161	250 kW/Phase

Table 6
Case C.

Bus 32	400 kW/Phase	Bus 52	550 kW/Phase
Bus 80	550 kW/Phase	Bus 123	350 kW/Phase
Bus 136	450 kW/Phase	Bus 161	250 kW/Phase

The power quality enhancement result is shown in Fig. 12. As seen from the figure, both the ESS-only and PV + ESS achieve significant

Table 7
The configuration cost.

	C_{LCC}^{E}	C_{Loss}	C_{Q}^{PV}	C_{all}
Case A	3.8374×10^6	4.7214×10^5	1.1604×10^5	4.4229×10^6
Case B	5.1881×10^6	4.125×10^5	0	5.6006×10^6
Case C	5.0754×10^6	4.6387×10^5	0	5.5392×10^6

power quality improvement, with comparable performance. Before optimization, the minimum voltage is below 0.95p.u. for extended periods. After applying the ESS, voltage is maintained steadily above 0.95p.u., thus avoiding low voltage occurrences. Prior to optimization, the maximum total harmonic distortion exceeded 6 %, whereas after optimization, total harmonic distortion is effectively suppressed to below 3 %. Power loss and voltage unbalance are also suppressed, which are not detailed here.

In terms of economic performance, this study compares the cost of ESS configuration required under three different scenarios: Case A, which considers the power quality compensation capability of PV; Case B, which ignores the power quality compensation capability of PV; and Case C, which ignores the power quality enhancement in ESS configuration. Table 5 and Table 6 present the ESS configuration results for Case B and Case C, respectively, while Table 7 shows the costs for all three cases. According to Table 7, it can be seen that the total cost in Case A is 21.03 % lower than that of Case B, indicating that considering the power quality compensation capability of PV leads to more economical ESS configuration. In contrast, the total cost in Case C is only 1.096 % lower than that of Case B, suggesting that including power quality indices, such as harmonics, in ESS configuration has a limited impact on the cost but contributes significantly to maintaining a higher power quality in the ADNs.

4.4. Comparison with other OPF model solutions

The proposed lower-level OHPF solving method is compared with conventional approaches, such as the nonlinear solver FMINCON and the convex optimization solver MOSEK. Due to the large scale and non-convex nature of the original OHPF model, the convex solver MOSEK cannot directly handle the problem. Therefore, for a simplified OPF problem with harmonics removed, a commonly used first-order Taylor linearization method is applied to convexify the model, which is then solved using MOSEK. The computational time required by the three methods is summarized in Table 8. As shown, solving the non-convex problem directly using FMINCON requires significantly more time than the proposed method. Although the convexified problem solved by MOSEK exhibits the shortest computation time, this approach is incapable of handling OHPF problems that include harmonics. In contrast, the proposed method not only offers superior computational efficiency but also effectively accounts for harmonics in the optimization process.

4.5. Comparison with the convex model

To evaluate the error introduced by the convex optimization method, we have calculated the maximum relative error between the convex model solution and the original nonconvex solution from power flow. The relative errors of power loss (e_{PL}), total harmonic distortion (e_{THD}),

Table 8
Time cost comparison.

Solver	Time cost (s)			
	0 h	6 h	18 h	20 h
FMINCON	532.74	514.63	568.92	587.16
First-order Taylor approximation + MOSEK	4.21	2.19	4.65	4.84
The proposed method	13.47	14.31	13.92	14.78

Table 9
Relative errors between the convex model and power flow.

iterations	e_{PL}	e_{THD}	e_u	e_U	e_I	e_h
1	0.0981	0.1640	0.0488	0.1060	19.5099	0.0656
2	0.0032	0.0539	0.0862	0.0198	0.8597	0.0008
3	0.0006	0.0067	0.0195	0.0035	0.1433	0.0011
4	0.0006	0.0005	0.0058	0.0009	0.0238	0.0001
5	0.0001	0.0007	0.0002	0.0006	0.0134	8×10^{-6}
6	0.0001	0.0005	0.0016	0.0005	0.0045	3×10^{-6}
7	0.0001	0.0004	0.0021	0.0004	0.0012	0
8	0.0001	0.0004	0.0022	0.0004	0.0003	0
9	0.0001	0.0004	0.0022	0.0004	9×10^{-5}	0
10	0.0001	0.0004	0.0023	0.0004	2×10^{-5}	0
11	0.0001	0.0004	0.0023	0.0004	7×10^{-6}	0
12	0.0001	0.0004	0.0023	0.0004	2×10^{-6}	0
13	0.0001	0.0004	0.0023	0.0004	2×10^{-6}	0

voltage unbalance (e_u), voltage (e_U), and current (e_I), and the constraint violation degree (e_h), are defined in (45).

$$e_m = \begin{cases} \max\limits_{\omega \in \Omega_m} \left| \dfrac{x_m^C(\omega) - x_m^P(\omega)}{x_m^P(\omega)} \right|, m \in \{PL, THD, u, U, I\} \\ \max\{h - \overline{h}, 0\}, m = h \end{cases} \tag{45}$$

where the superscripts C and P denote the convex model state variables and the power flow results, respectively. For the inequality constraint $h(x)$, h and $\overline{h}$ denote the constraint value and its bound. The results are summarized in Table 9 and Fig. 13.

As shown in Table 9 and Fig. 13, noticeable discrepancies appear between the convex model solution and the power flow results during the initial iterations. As the number of iterations increases, the error gradually decreases, and the convex model solution becomes very close to that of the original model, thereby verifying the effectiveness of the proposed iterative scheme.

4.6. Comparison with different PV penetration levels

To investigate different PV penetration levels, the initial 50 kW of PV per phase is incrementally increased by 50 kW steps up to 400 kW in order. The corresponding ESS capacity optimization result is shown in Fig. 14. From the figure, it can be observed that when the PV penetration is low, such as with a per-phase PV power of 50 kW to 200 kW, the daytime PV output peak can adequately compensate for the midday load peak. When there is no voltage violation, the ESS power requirement is relatively low. During nighttime when PV generation is unavailable, the increase in PV penetration enhances the available dispatchable power margin, thus reducing the ESS's support requirement for power quality. Therefore, when the overall PV penetration is relatively low, the total ESS power demand decreases to a minimum value as PV penetration increases. At this time, the ESS is primarily used to maintain voltage stability and mitigate harmonic distortion. However, when the connected PV power rises to 250 kW, 300 kW, or higher penetration levels, excess PV integration leads to a significant increase in reverse power flow, resulting in severe voltage violations. This forces the ESS power demand to increase continuously to support power quality compensation. Although the dispatchable power margin increases during nighttime, the savings in ESS power cannot offset the substantial increase in ESS power quality compensation costs during the day, which ultimately causes the total ESS power demand to increase as PV penetration rises. Therefore, as the PV penetration rate gradually increases, the required ESS power initially decreases and then increases.

4.7. Impact of different RPC

The economic viability of PV-ESS coordination depends critically on the compensation pricing mechanism. In Section IV-C, a fixed *RPC* of 1.5 % of the TOU price is used. This section evaluates the impact of

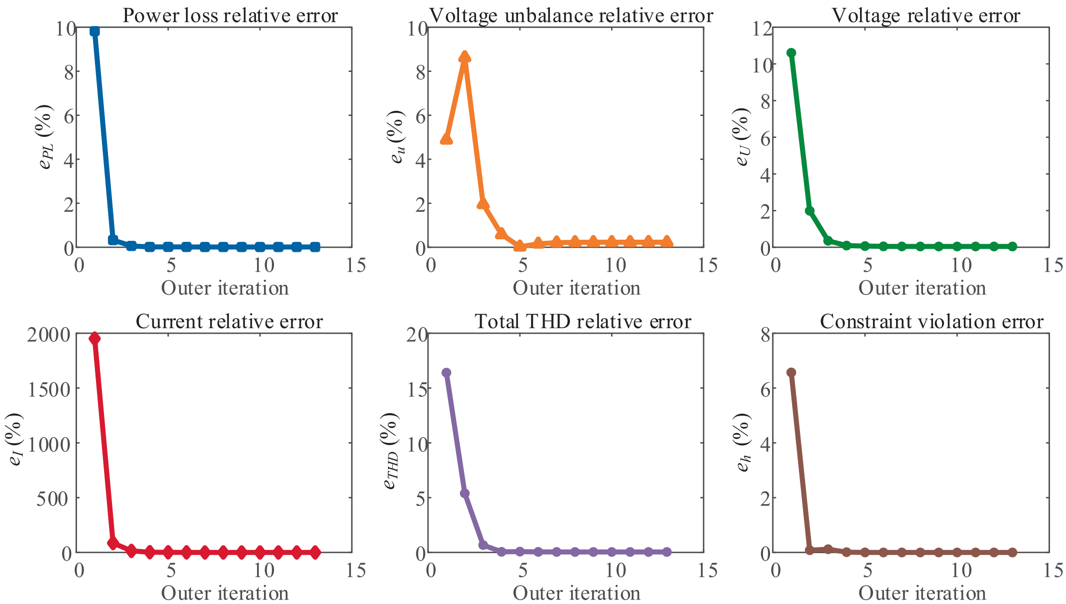

Fig. 13. Relative errors between the convex model and power flow.

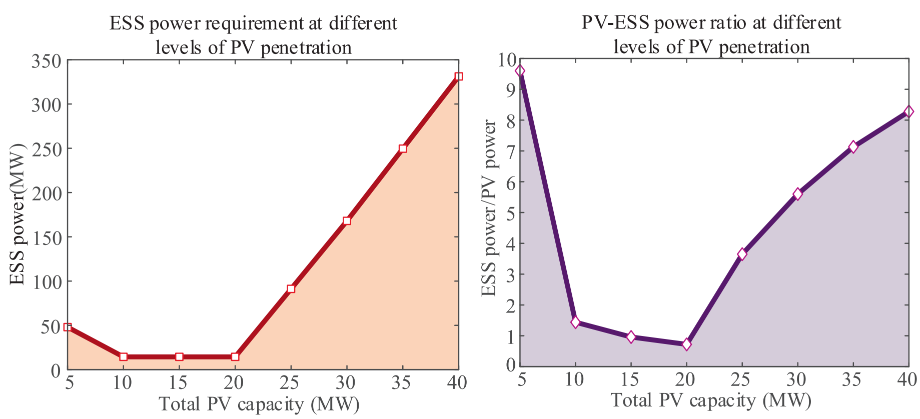

Fig. 14. ESS power requirement under different levels of PV penetration

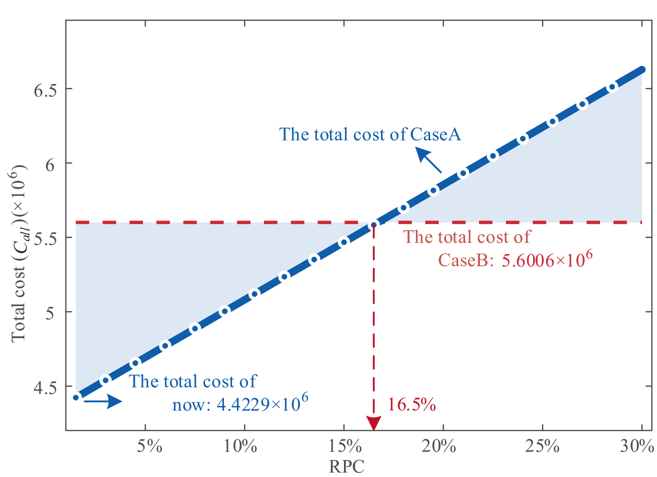

Fig. 15. Trend of total cost (C_{all}) variation with *RPC* changes.

varying *RPC* values on the economic conclusions, as shown in Fig. 15. As *RPC* increases, PV compensation cost rises, directly affecting the total cost of Case A. When *RPC* is below 16.5 % of the TOU price, Case A exhibits higher economic efficiency; however, with further increases in *RPC*, Case A loses economic feasibility because the rising PV compensation cost outweighs the ESS installation cost savings achieved through PV scheduling.

Therefore, over a range of *RPC* values, the proposed method remains economically efficient provided that the PV compensation cost stays below the savings in ESS configuration cost. In practice, increasing the *RPC* can provide greater compensation to participants and further encourage participation in power quality services via PV.

5. Conclusion

This study presents a bi-level optimization framework for ESS configuration in ADNs incorporating coordinated operation with PV systems. The framework effectively mitigates key power quality challenges, such as voltage fluctuations, harmonic distortions, and three-phase imbalances, thereby enhancing overall grid stability and performance. A significant advantage of the proposed method lies in its ability to handle complex power quality constraints while maintaining computational efficiency. Specifically, the upper-level model selects candidate nodes based on their contribution to power quality indices, thereby narrowing down the configuration space, while the lower-level model transforms the power flow equations into current injection equations, further reformulating the MPOHPF problem into a convex quadratic constrained quadratic program solved by an alternating iterative algorithm.

The effectiveness of the proposed bi-level optimization model and solving method has been verified using a 162-node three-phase four-wire distribution network. The results demonstrate that the proposed ESS configuration strategy can effectively reduce the power loss while limiting the voltage deviation, harmonic distortion, and unbalance within the standard limits. The economic analysis reveals that considering the power quality compensation capability of PV significantly improves the cost-effectiveness of ESS configuration, achieving a 21.03 % reduction in total cost compared to the scenario where PV's compensation ability is disregarded. In contrast, when the impact of power quality enhancement is excluded from the ESS configuration process, the cost reduction is only 1.096 %, indicating that including power quality indices, such as harmonics, in the ESS configuration has a limited impact on cost but contributes significantly to maintaining higher power quality in the ADNs.

In this study, ESS configuration is implemented within ADNs at a single voltage level. Future work will use hierarchical coordination to integrate conventional voltage regulation methods, such as transformer tap changers, into the coordinated management framework of ESS and PV, thereby enabling power quality control across multi-level power grids. In addition, future work will incorporate more extreme scenarios such as line faults and line switching into ESS configuration and develop a dynamic candidate node selection method to enhance the reliability of the configuration.

CRediT authorship contribution statement

Yang Wang: Writing – review & editing, Writing – original draft, Validation, Methodology, Investigation, Conceptualization. **Jiaqi Duan:** Writing – review & editing, Writing – original draft, Validation, Methodology, Investigation. **Zhuocheng Li:** Validation, Supervision, Resources, Methodology. **Xianyong Xiao:** Writing – review & editing, Supervision, Resources. **Xiang Zhou:** Writing – review & editing, Validation, Software. **Hengchen Yang:** Software, Data curation. **Jiajia Yang:** Visualization, Software.

Declaration of competing interest

The authors declare that they have no known competing financial interests or personal relationships that could have appeared to influence the work reported in this paper.

Acknowledgements

This work was supported by the National Key R&D Program of China (2023YFB2407600).

Data availability

Data will be made available on request.

References

[1] Mahela OP, Shaik AG. Power quality improvement in distribution network using DSTATCOM with battery energy storage system. Int J Electr Power Energy Syst 2016;83:229–40.
[2] Ma W, Wang W, Chen Z, Hu R. A centralized voltage regulation method for distribution networks containing high penetrations of photovoltaic power. Int J Electr Power Energy Syst 2021;129:106852.
[3] Santos A, Duggan GP, Young P, Frank S, Hughes A, Zimmerle D. Harmonic cancellation within AC low voltage distribution for a realistic office environment. Int J Electr Power Energy Syst 2022;134:107325.
[4] Alabri W, Jayaweera D. Voltage regulation in unbalanced power distribution systems with residential PV systems. Int J Electr Power Energy Syst 2021;131:107036.
[5] Takagi M, Fukushima K, Tagashira N, Okada K, Asano H. Cost-effectiveness analysis method for voltage stabilization in case of combining storage battery and reactive power compensator. J Storage Mater 2024;93:112065.
[6] Hosseinpour H, Bastaee B. Optimal placement of on-load tap changers in distribution networks using SA-TLBO method. Int J Electr Power Energy Syst 2015;64:1119–28.
[7] Rezapour H, Fathnia F, Fiuzy M, Falaghi H, Lopes AM. Enhancing power quality and loss optimization in distorted distribution networks utilizing capacitors and active power filters: a simultaneous approach. Int J Electr Power Energy Syst 2024;155:109590.
[8] Wan L, Yang J, Yang Y, Li T, Liu H, Wen F. Optimal sizing and operation of community hybrid energy storage systems. J Storage Mater 2025;119:116209.
[9] Rahimipour Behbahani M, Karimi H. Multi-objective operation of renewable multi-microgrids integrated with energy storage system considering power losses and harmonics. J Storage Mater 2025;117:116128.
[10] Xiao X, Li Z, Wang Y, Zhou Y, Liu K. Optimal power quality compensation of energy storage system in distribution networks based on unified multi-phase OPF model. IEEE Trans Smart Grid 2022;13:1873–87.
[11] Rowe K, Mokryani G, Cooke K, Campean F, Chambers T. Bi-level optimal sizing, siting and operation of utility-scale multi-energy storage system to reduce power losses with peer-to-peer trading in an electricity/heat/gas integrated network. J Storage Mater 2024;83:110738.
[12] Shao J, Chen H, Çelik Ö, Wei B, Vasquez JC, Guerrero JM. Trade-off both in the clearing market and ancillary services markets for agriculture park operator: a strategic bilevel multi-objective programming. Appl Energy 2025;388:125634.
[13] Mahdavi S, Hemmati R, Jirdehi MA. Two-level planning for coordination of energy storage systems and wind-solar-diesel units in active distribution networks. Energy 2018;151:954–65.
[14] Chen C, Sun H, Shen X, Guo Y, Guo Q, Xia T. Two-stage robust planning-operation co-optimization of energy hub considering precise energy storage economic model. Appl Energy 2019;252:113372.
[15] Li R, Wang W, Wu X, Tang F, Chen Z. Cooperative planning model of renewable energy sources and energy storage units in active distribution systems: a bi-level model and pareto analysis. Energy 2019;168:30–42.
[16] Jiang X, Jin Y, Zheng X, Hu G, Zeng Q. Optimal configuration of grid-side battery energy storage system under power marketization. Appl Energy 2020;272:115242.
[17] Ma M, Huang H, Song X, Peña-Mora F, Zhang Z, Chen J. Optimal sizing and operations of shared energy storage systems in distribution networks: a bi-level programming approach. Appl Energy 2022;307:118170.
[18] Fawzy S, Abd-Raboh EE, El-Afifi MI, Eladl AA. Optimal location and operation of energy storage and transmission switching for minimizing wind power spillage. J Storage Mater 2024;90:111925.
[19] Zhu Y, Wei J, Wang B, Hong S, Liu Y, Lu L. Optimal robust sizing of distributed energy storage considering power quality management. IET Renew Power Gener 2024;18:3825–38.
[20] Rohani, A., Abasi, M., Beigzadeh, A., Joorabian, M., B. Gharehpetian, G., 2021. Bi-level power management strategy in harmonic-polluted active distribution network including virtual power plants. IET Renewable Power Generation 15, 462–476.
[21] Alrashidi M, Rahman S. A bi-level optimization method for voltage control in distribution networks using batteries and smart inverters with high wind and photovoltaic penetrations. Int J Electr Power Energy Syst 2023;151:109217.
[22] Zhang J, Zhu L, Zhao S, Yan J, Lv L. Optimal configuration of energy storage systems in high PV penetrating distribution network. Energies 2023;16.
[23] Li J, Yang B, Huang J, Guo Z, Wang J, Zhang R, et al. Optimal planning of electricity–hydrogen hybrid energy storage system considering demand response in active distribution network. Energy 2023;273:127142.
[24] Babacan O, Torre W, Kleissl J. Siting and sizing of distributed energy storage to mitigate voltage impact by solar PV in distribution systems. Sol Energy 2017;146:199–208.
[25] Salee, S., Wirasanti, P., 2018. Optimal siting and sizing of battery energy storage systems for grid-supporting in electrical distribution network, in: 2018 International ECTI Northern Section Conference on Electrical, Electronics, Computer and Telecommunications Engineering (ECTI-NCON). Presented at the 2018 International ECTI Northern Section Conference on Electrical, Electronics, Computer and Telecommunications Engineering (ECTI-NCON), pp. 100–105.
[26] Das CK, Bass O, Kothapalli G, Mahmoud TS, Habibi D. Overview of energy storage systems in distribution networks: placement, sizing, operation, and power quality. Renew Sustain Energy Rev 2018;91:1205–30.
[27] Prakash P, Khatod DK. Optimal sizing and siting techniques for distributed generation in distribution systems: a review. Renew Sustain Energy Rev 2016;57:111–30.
[28] Martín García JA, Gil Mena AJ. Optimal distributed generation location and size using a modified teaching–learning based optimization algorithm. Int J Electr Power Energy Syst 2013;50:65–75.
[29] Lu T, Ai Q, Wang Z. Interactive game vector: a stochastic operation-based pricing mechanism for smart energy systems with coupled-microgrids. Appl Energy 2018;212:1462–75.
[30] Adoum Abdoulaye M, Waita S, Wabuge Wekesa C, Mwabora JM. Optimal sizing of an off-grid and grid-connected hybrid photovoltaic-wind system with battery and fuel cell storage system: a techno-economic, environmental, and social assessment. Appl Energy 2024;365:123201.
[31] Liu Y, Li J, Wu L. ACOPF for three-phase four-conductor distribution systems: Semidefinite programming based relaxation with variable reduction and feasible solution recovery. IET Generation, Transmission & Distribution 2019;13:266–76.

[32] Chen T, Song Y, Hill DJ, Lam AYS. Chance-constrained OPF in droop-controlled microgrids with power flow routers. IEEE Trans Smart Grid 2022;13:2601–13.
[33] López JC, Franco JF, Rider MJ, Romero R. Optimal restoration/maintenance switching sequence of unbalanced three-phase distribution systems. IEEE Trans Smart Grid 2018;9:6058–68.
[34] Long J, Yang Z, Zhao J, Yu J. Modular linear power flow model against large fluctuations. IEEE Trans Power Syst 2024;39:402–15.
[35] Stai E, Wang C, Le Boudec J-Y. On the solution of the optimal power flow for three-phase radial distribution networks with energy storage. IEEE Trans Control Netw Syst 2021;8:187–99.
[36] Zakeri B, Syri S. Electrical energy storage systems: a comparative life cycle cost analysis. Renew Sustain Energy Rev 2015;42:569–96.
[37] Amini M, Nazari MH, Hosseinian SH. Optimal energy management of battery with high wind energy penetration: a comprehensive linear battery degradation cost model. Sustain Cities Soc 2023;93:104492.
[38] Abdelrahman S, Milanović JV. Practical approaches to assessment of harmonics along radial distribution feeders. IEEE Trans Power Delivery 2019;34:1184–92.
[39] Liu J, Wei X, Huang H. An improved grey wolf optimization algorithm and its application in path planning. IEEE Access 2021;9:121944–56.
[40] Fesli U, Ozdemir MB, Akın M. Grey wolf algorithm-based source size and location determination method for capacity expansion planning in power systems. Engineering Science and Technology, an International Journal 2025;61:101934.
[41] Bu, F., Yuan, Y., Wang, Z., Dehghanpour, K., Kimber, A., 2019. A Time-Series Distribution Test System Based on Real Utility Data, in: 2019 North American Power Symposium (NAPS). Presented at the 2019 North American Power Symposium (NAPS), IEEE, Wichita, KS, USA, pp. 1–6.
[42] Xiao X, Li Z, Wang Y, Zhou Y. A Practical Approach to Estimate Harmonic Distortions in Residential distribution System. IEEE Trans Power Delivery 2021;36:1418–27.
[43] Huang ZF, Chen WD, Wan YD, Shao YL, Islam MR, Chua KJ. Techno-economic comparison of different energy storage configurations for renewable energy combined cooling heating and power system. Appl Energy 2024;356:122340.
[44] Shabani M, Wallin F, Dahlquist E, Yan J. The impact of battery operating management strategies on life cycle cost assessment in real power market for a grid-connected residential battery application. Energy 2023;270:126829.
[45] Mahuze RA, Amadeh A, Yuan B, Zhang KM. Collaborative optimization framework for capacity planning of a prosumer-based peer-to-peer electricity trading community. Appl Energy 2025;384:125289.